

Analysis of nanopore arrangement and structural features of anodic alumina layers formed by two-step anodizing in oxalic acid using the dedicated executable software

Leszek Zaraska · Wojciech J. Stępniewski ·
Grzegorz D. Sulka · Eryk Ciepiela · Marian Jaskuła

Received: 14 January 2013 / Accepted: 6 February 2013 / Published online: 15 February 2013
© The Author(s) 2013. This article is published with open access at Springerlink.com

Abstract Anodic porous alumina layers were fabricated by a two-step self-organized anodization in 0.3 M oxalic acid under various anodizing potentials ranging from 30 to 60 V at two different temperatures (10 and 17 °C). The effect of anodizing conditions on structural features and pore arrangement of AAO was investigated in detail by using the dedicated executable publication combined with ImageJ software. With increasing anodizing potential, a linear increase of the average pore diameter, interpore distance, wall thickness and barrier layer thickness, as well as a decrease of the pore density, were observed. In addition, the higher pore diameter and porosity values were obtained for samples anodized at the elevated temperature, independently of the anodizing potential. A degree of pore order was investigated on the basis of Delaunay triangulations (defect maps) and calculation of pair distribution or angle distribution functions (PDF or ADF), respectively. All methods confirmed that in order to obtain nanoporous alumina with the best, hexagonal pore arrangement, the potential of 40 V should be applied during anodization. It was confirmed that the dedicated executable publication can be used to a fast and complex

analysis of nanopore arrangement and structural features of nanoporous oxide layers.

1 Introduction

Recently, anodic porous alumina attracted much attention because of its numerous applications in materials of science and nanotechnology [1]. To gain new properties of materials related to their nanometric size in at least one dimension, nanowires [2–11], nanotubes [12, 13] and nanodots [14, 15] made of various materials like metals and alloys [2–5, 14, 15], semiconductors [6, 7], superconductors [8] and polymers [10–13] were obtained using various techniques, including electrochemical deposition [2–5, 10–12], sol–gel technique [6, 8], atomic layer deposition [14, 15], and chemical vapor deposition [9]. Recently, fabrication of many devices based on anodic aluminum oxide (AAO) has been also reported [16–19]. Since a strict control of nanopore geometry and arrangement is often crucial for properties of final products based on AAO, much effort has to be implemented to investigate this subject and to develop novel methods and tools for materials characterization.

In general, anodic porous alumina for nanotechnology applications can be obtained in two ways: by anodization of pre-textured aluminum and by self-organized two-step anodization [20]. Electropolished aluminum can be pre-textured using various techniques, including atomic force microscopy (AFM) [21] and scanning probe microscopy (SPM) [22]. To save time and effort, molds usually made of materials like SiC [23–26], Si₃N₄ [27] or Ni [28], manufactured by lithographic techniques, were applied for the aluminum pre-texturation. Due to the pre-texturing process one can obtain defect-free hexagonally arranged nanoporous alumina [24], squarely arranged circular pores [25], and

L. Zaraska (✉) · G.D. Sulka · M. Jaskuła
Department of Physical Chemistry and Electrochemistry, Faculty of Chemistry, Jagiellonian University, Ingardena 3,
30-060 Krakow, Poland
e-mail: zaraska@chemia.uj.edu.pl
Fax: +48-12-6340515

W.J. Stępniewski
Department of Advanced Materials and Technologies, Faculty of Advanced Technology and Chemistry, Military University of Technology, Gen. Sylwestra Kaliskiego 2, 00-908 Warsaw, Poland

E. Ciepiela
Academic Computer Centre CYFRONET, AGH University of Science and Technology, Nawojki 11, 30-950 Krakow, Poland

square or triangular nanopores [26]. The main disadvantage of the pre-texturation is that it is based on expensive and time consuming methods. The pre-textured alumina surface limited up to few square millimeters is also a discouraging drawback. On the other hand, self-organized anodization eliminates these types of problems, but it does not provide a defect-free arrangement of nanopores [20].

The most common electrolytes for self-organized anodization are sulfuric acid [29–31], oxalic acid [32–35] and phosphoric acid [36–38]. Anodizing potential, a crucial factor that governs the arrangement of nanopores and their geometry is strictly related to the electrolyte. For example, one can anodize aluminum in sulfuric acid up to 25 V [29]. At potentials above this, usually electrochemical dissolution of the anode occurs; however, there are individual exceptions and aluminum can be anodized in sulfuric acid even at 32 V [39]. Anodization in oxalic acid is usually conducted at 40 V, providing the best arrangement of the hexagonal array of nanopores [33, 35]. However, anodization at higher potentials, known as hard anodization, has been also reported [34]. A mild anodization of aluminum in phosphoric acid can be carried out at up to 195 V [20].

In the present study, the influence of operating conditions (especially anodizing potential) on the structural features of nanoporous alumina and degree of pore order has been investigated by using the new, dedicated computational experiment [40] powered by the GridSpace2 Web-based distributed computing platform [41], published as an executable publication [42] using Collage Authoring Environment [43]. The changes in pore diameter and interpore distance of AAOs with applied potential during anodization were investigated in detail. This study provides data that might be useful for further fabrication of nanostructured materials with defined diameters, spacing and arrangement. Moreover, the nanopore arrangement was examined by various methods, including defect maps, known as Delaunay triangulations, and quantitative analyses based on a pair distribution function (PDF) and angular distribution function (ADF).

2 Experimental

A high purity (99.9995 %), annealed aluminum foil purchased from Alfa-Aesar was cut into specimens (2.5 cm × 0.5 cm) with working area of 0.5 cm². Then, aluminum was degreased in acetone and ethyl alcohol and electropolished in a 1:4 vol. mixture of HClO₄ and C₂H₅OH at constant current density of 0.5 A cm⁻² at 10 °C for 1 min. The samples were anodized in a 0.3 M oxalic acid solution for 14 h, under various anodizing potentials ranging from 30 to 60 V. Two series of experiments were performed at different temperatures (10 and 17 °C). After anodization, anodic aluminum

oxide was chemically removed from the metal surface by etching in a mixture of 6 wt.% H₃PO₄ and 1.8 wt.% H₂CrO₄ at 60 °C for 2 h. The second anodization was carried out under the same experimental conditions as were used during the first anodizing step. In order to keep the constant electrolyte temperature, all anodization procedures were carried out in a double-walled electrochemical cell combined with a refrigerated circuiting system (Thermo Haake, DC10–K15). A Pt grid was used as a cathode and a distance between both electrodes was about 2 cm. The morphology of the samples was evaluated by a field emission scanning electron microscope (FE-SEM, Hitachi S-4700). The structural features of alumina layers and degree of pore order were estimated directly from SEM images by using ImageJ 1.37v software [44], and the dedicated computational experiment and corresponding executable publication powered by the GridSpace2 platform [41] and Collage Authoring Environment [43].

3 Results and discussion

In order to perform a detailed inspection of structural features of as-obtained porous anodic alumina layers, all nanopores in the SEM image were firstly identified by ImageJ software [44]. During this step, such parameters as area, circularity and center of mass coordinates were determined for each pore. Next, the dedicated executable publication [40, 42] was employed to calculate the average pore diameter (D_p), interpore distance (D_c), circularity of pores and a percentage of defective pores. The effect of anodizing potential on pore diameter and interpore distance of anodic porous alumina synthesized by anodization at different temperatures is shown in Fig. 1a and b, respectively.

In general, pore diameter increases linearly with increasing anodizing potential, and this fact is in excellent agreement with the literature data [20]. The generally accepted dependence between anodizing potential and pore diameter, proposed by O'Sullivan and Wood, is shown in Fig. 1a by a blue dashed line [45]. Slightly lower proportionality constants, compared to this proposed by O'Sullivan and Wood (see Table 1), could be attributed to the fact that an average pore diameter is affected not only by anodizing potential but also by other anodizing parameters such as electrolyte concentration and temperature. The influence of anodizing temperature is clearly visible in Fig. 1a. For anodization carried out at the higher temperature, alumina layers with larger nanopores were obtained as a consequence of enhanced field-assisted dissolution of aluminum oxide and more effective chemical etching of outer oxide layer by acidic electrolyte. A much lower average pore size observed for the samples anodized at 17 °C and 60 V is a result of the low degree of pore order (see below) and complex structure of pores with formed sub-pores underneath the surface.

Fig. 1 Pore diameter (a) and interpore distance (b) as a function of anodizing potential

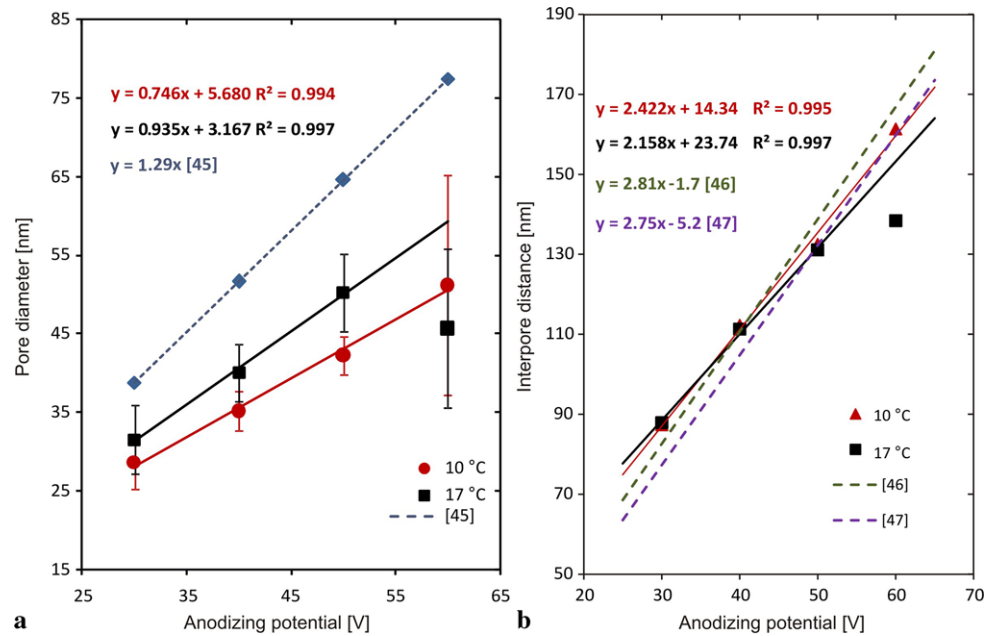


Table 1 The proportionality constant (λ_p) between the pore diameter and anodizing potential for various anodizing temperatures

Anodizing temperature	Proportionality constant λ_p [nm V ⁻¹]
10 °C	0.88
17 °C	1.05
Literature value [45]	1.29

As can be seen in Fig. 1b, the average interpore distance (cell diameter) is also linearly dependent on anodizing potential. The similar relations were obtained by many research groups for different electrolytes [20]. For instance, the empirical relations obtained for anodization performed in oxalic acid by Ebihara et al. [46], and Hwang et al. [47] are also plotted in Fig. 1b respectively as green and purple dashed lines. As previously mentioned, the lower value of the average interpore distance observed for 17 °C and 60 V is also a result of the complex structure of disordered nanopores. As shown in Fig. 1b, the interpore distance was found to be almost independent of the temperature of anodization, which is in general agreement with the data obtained by Hwang et al. [47], and Stępniewski and Bojar [48].

The effect of anodizing potential on wall thickness (W) and thickness of dielectric oxide layer at the pore bottoms called the barrier layer (B) is shown in Fig. 2. The wall thickness was calculated from the well-known equation derived for an ideal hexagonal pore arrangement [20].

$$W = (D_c - D_p)/2 \quad (1)$$

On the other hand, according to Ebihara et al., the barrier layer thickness is related directly to the wall thickness and

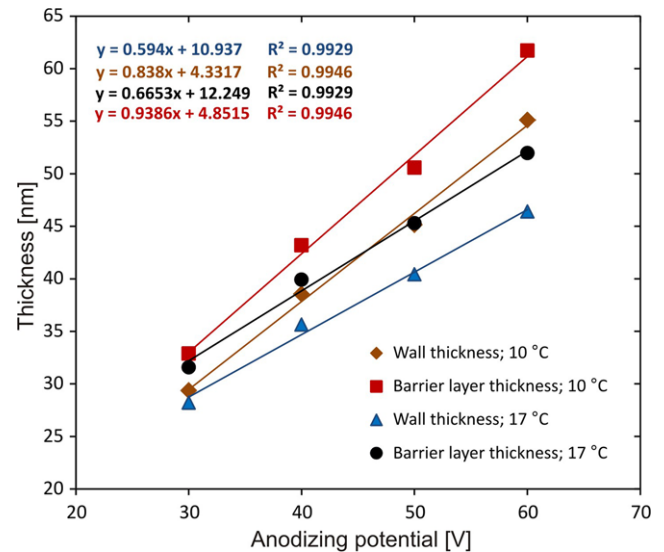


Fig. 2 The dependence between wall thickness and barrier layer thickness on potential applied during anodization

can be calculated from the empirical equation (2) established for anodizations carried out in oxalic acid [46].

$$B = 1.12 \cdot W \quad (2)$$

It should be mentioned that the thickness of this continuous dielectric oxide layer on the pore bottoms is a key factor that affects further applications of anodic alumina membrane as a template for nanofabrication. It can be seen in Fig. 2 that the higher potential applied during anodization, the thicker cell walls and barrier layer are formed. In addition, increasing temperature of anodization results in a decrease of W and B values. It can be attributed to the enhanced field-

assisted dissolution of alumina at the oxide/electrolyte interface at elevated temperatures.

Other two parameters often used for characterization of nanoporous anodic alumina layers are pore density (n), defined as number of pores on the surface area of 1 cm^2 , and porosity (α), defined as a ratio of a surface area occupied by pores to the total surface area of oxide. For all anodized samples, values of these parameters were calculated from well-known equations (3) and (4) established for hexagonally arranged nanoporous structures [20].

$$n = \frac{2 \cdot 10^{14}}{\sqrt{3} \cdot D_c^2} \quad (3)$$

$$\alpha = \frac{\pi}{2\sqrt{3}} \cdot \left(\frac{D_p}{D_c}\right)^2 \quad (4)$$

The influence of anodizing potential on the pore density and porosity is respectively illustrated in Fig. 3a and b. It is clearly visible that the pore density decreases exponentially with increasing anodizing potential (Fig. 3a) independently of the anodizing temperature. This trend, as a direct consequence of Eq. (3), is a result of the linear dependence of interpore distance on potential applied during anodization. The results in Fig. 3b show that the porosity of anodic alumina remains almost constant with increasing anodizing potential for anodization procedures carried out at $10 \text{ }^\circ\text{C}$. For the anodizing temperature of $17 \text{ }^\circ\text{C}$, a noticeable increase in the porosity is observed when the anodizing potential increases from 40 to 50 V. Moreover, the higher porosity values were obtained for samples anodized at the elevated temperature, independently of the anodizing potential. This is obviously also a result of the temperature-enhanced rate of effective etching of aluminum oxide by the electrolyte.

The effect of anodizing potential on degree of pore order and regularity of the nanoporous structures was also investigated in detail by using different methods. At first, pore shape was analyzed by calculating a circularity coefficient defined as

$$\text{circ.} = 4\pi \left(\frac{S}{\text{perimeter}^2} \right) \quad (5)$$

where S is a surface area occupied by a single pore. The circularity value close to 0.0 indicates that the pore is an elongated polygon, while value 1.0 is observed when the pore is ideally circular. The average circularity coefficients calculated for all studied samples are shown in Fig. 4a. As can be seen, for both studied temperatures, the highest pore circularity is observed for anodization procedures carried out at 40 V. Moreover, on raising the temperature from 10 to $17 \text{ }^\circ\text{C}$, the pore circularity increases independently of the applied potential due to the more effective isotropic

etching of aluminum oxide at the oxide/electrolyte interface.

To construct defect maps known as Delaunay triangulations, the dedicated executable publication [42] was employed. The pores that were not six-fold coordinated by neighboring pores were recognized as defect and marked in black. The SEM images of two different samples anodized at 30 and 40 V, together with the corresponding defect maps combined with visual pore representations constructed on the basis of color coding algorithm described in our previous work [40], are shown in Fig. 5 and Fig. 6, respectively.

As can be seen, much less defective pores can be found in the sample anodized at 40 V. The defect percentage, defined as a ratio between the number of defective pores and number of all pores on the analyzed surface, was also calculated for all samples. The results (Fig. 4b) clearly indicate that the optimal anodizing potential, at which the least defective nanoporous structure can be formed, is 40 V.

The pore order in AAO layers was also investigated on the basis of the pair distribution function (PDF), being the distribution of distances between pairs of pores, and the angular distribution function (ADF) [49]. For a long-range hexagonal order of pores, the PDF consists of sharp and well defined peaks and the position of the maximum of the first peak indicates an average interpore distance in the nanoporous lattice (Fig. 6d). On the contrary, when some disturbances in hexagonal arrangement of pores are present, peaks in the PDF profile become less intensive, wider and sometimes overlap each other (see Fig. 5d). On the other hand, for the hexagonal lattice the narrow ADF curve, centered around 60° , is observed (Fig. 6c). A non-ideal arrangement of pores provides a wider and asymmetrical ADF peak, clearly seen in Fig. 5c. For all anodized samples, regularity ratios based on the ADF and the first peak of the PDF, defined as a ratio of the peak maximum to the full width of the peak at half maximum, divided by the number of pores, were calculated. The results for the ADF-based regularity ratio (Fig. 4c) and the PDF-based regularity ratio (Fig. 4d) confirmed that the best hexagonal arrangement of pores in nanoporous alumina can be obtained when the potential of 40 V is applied during anodization. Our findings are in excellent agreement with the literature data [20], according to which the potential of 40 V is known as a self-ordering regime for anodization carried out in oxalic acid electrolytes.

4 Conclusions

In conclusion, the structural features and degree of pore order in nanoporous alumina synthesized in oxalic acid were analyzed by using the dedicated executable publication

Fig. 3 The dependence between pore density (a) and porosity (b) on anodizing potential

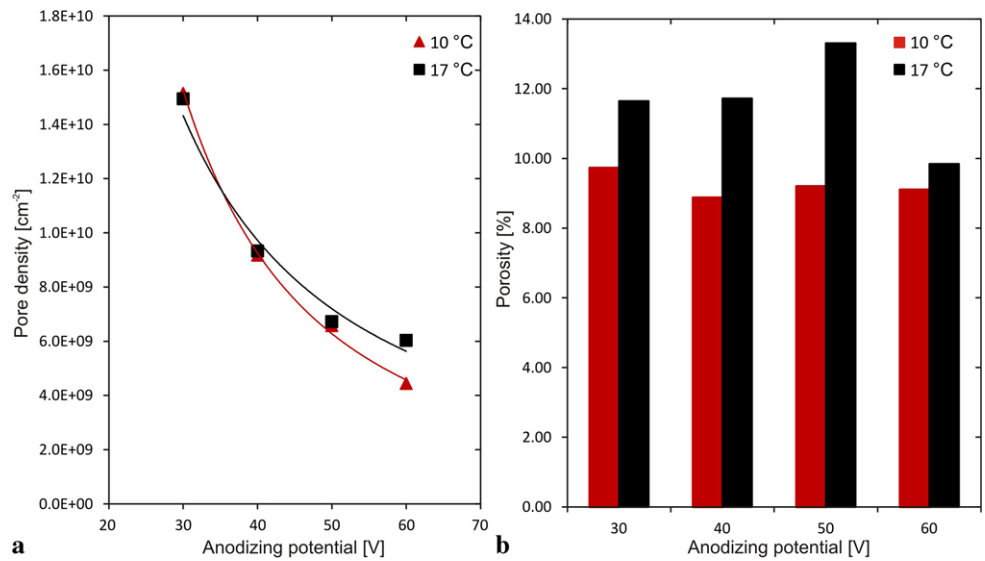
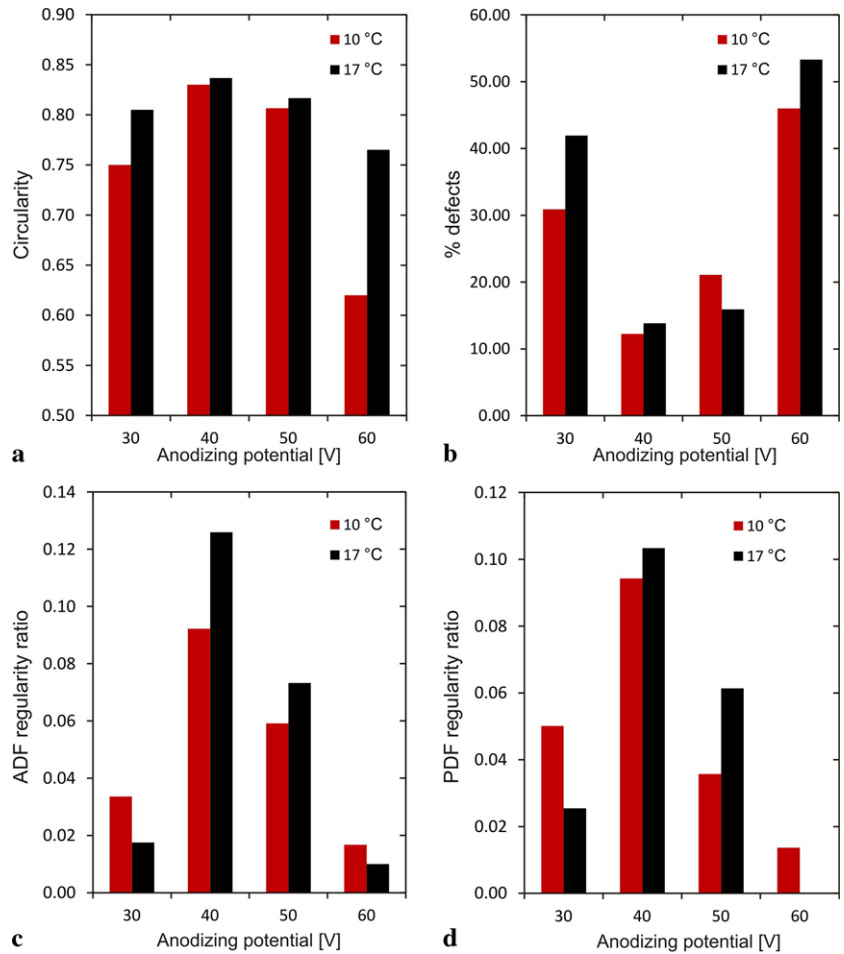


Fig. 4 Circularity coefficients (a), percentages of defects (b), ADF-based regularity ratios (c) and PDF-based regularity ratios (d) for all studied potentials and temperatures



combined with ImageJ software. It was found that parameters of nanoporous structures such as average pore diameter, interpore distance, wall thickness and barrier layer thickness increase linearly with increasing anodizing potential. The nanopore arrangement was investigated using various

methods, including the construction of defect maps known as Delaunay triangulations and calculation of pair distribution or angle distribution functions (PDF or ADF, respectively). It should be mentioned that the results based on proposed ADF- and PDF-based regularity ratios were in excel-

Fig. 5 SEM image (a) together with the defect map (b), ADF function (c) and PDF function (d) obtained for the sample anodized at 30 V

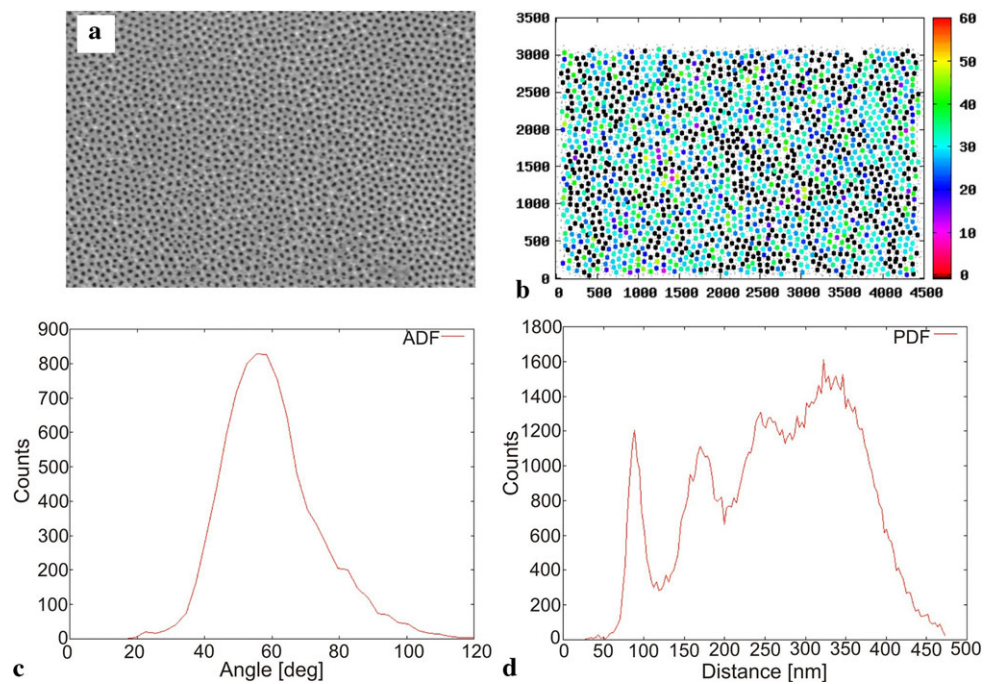
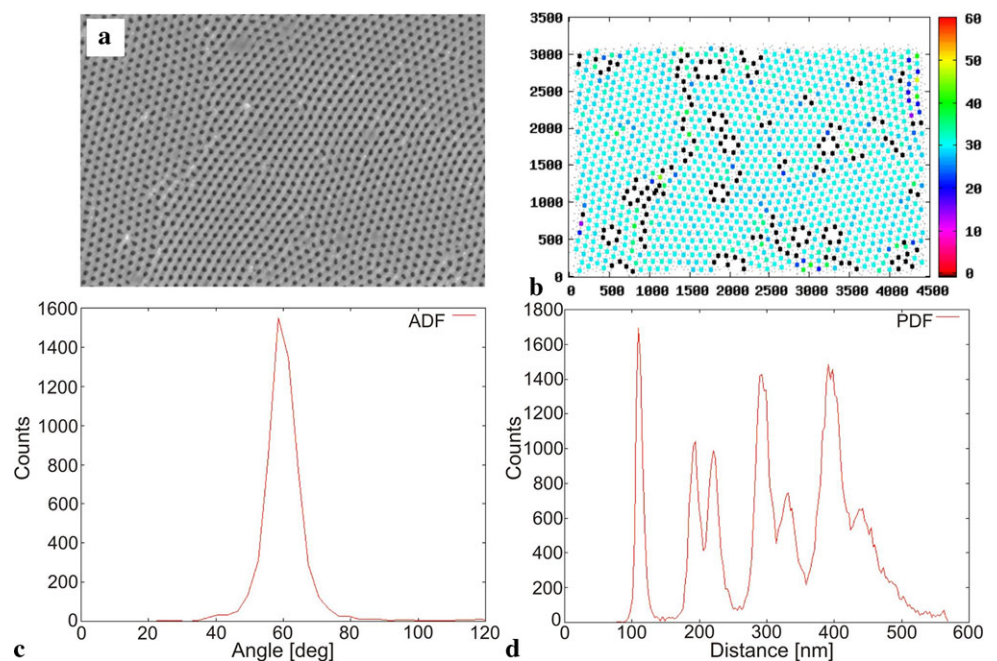


Fig. 6 SEM image (a) together with the defect map (b), ADF function (c) and PDF function (d) obtained for the sample anodized at 40 V



lent agreement with those obtained from the defect analysis. It was confirmed that the optimal anodizing potential that allows for the synthesis of almost ideal hexagonally arranged nanoporous alumina in oxalic acid is 40 V. The dedicated executable publication proposed in our previous works [40, 42] is a promising interactive tool that helps in fast and complex analysis of nanopore arrangement and structural features of nanoporous oxide layers. The tool can be successfully used for the analysis of order in nanoporous materials and arranged layers of nanoparticles.

Acknowledgements The SEM imaging was performed in the Laboratory of Field Emission Scanning Electron Microscopy and Microanalysis at the Institute of Geological Sciences, Jagiellonian University, Poland. This work was made possible with assistance of the PL-Grid project, contract number: POIG.02.03.00-00-007/08-00, website: www.plgrid.pl. The project is co-funded by the European Regional Development Fund as part of the Innovative Economy program.

Open Access This article is distributed under the terms of the Creative Commons Attribution License which permits any use, distribution, and reproduction in any medium, provided the original author(s) and the source are credited.

References

1. G.D. Sulka, L. Zaraska, W.J. Stępniewski, in *Encyclopedia of Nanoscience and Nanotechnology*, 2nd edn., vol. 11, ed. by H.S. Nalwa (American Scientific Publishers, Valencia, 2011), pp. 261–349
2. G.D. Sulka, A. Brzózka, L. Zaraska, M. Jaskuła, *Electrochim. Acta* **55**, 4368 (2010)
3. T. Ohgai, X. Hoffer, A. Fabian, L. Gravier, J.-P. Ansermet, *J. Mater. Chem.* **13**, 2530 (2003)
4. J. Qin, J. Nogue, M. Mikhaylova, A. Roig, J.S. Munoz, M. Muhammed, *Chem. Mater.* **17**, 1829 (2005)
5. D.S. Choi, Y. Rheem, B. Yoo, N.V. Myung, Y.K. Kim, *Curr. Appl. Phys.* **10**, 1037 (2010)
6. V. Gaponenko, I.S. Molchan, D.A. Tsykunov, G.K. Maliarevich, M. Aegerter, J. Puetz, N. Al-Dahoudi, J. Misiewicz, R. Kudrawiec, V. Lambertini, N. Li Pira, P. Repetto, *Microelectron. Eng.* **81**, 255 (2005)
7. S.P. Mondal, K. Das, A. Dhar, S.K. Ray, *Nanotechnology* **18**, 095606 (2007)
8. X. Jian, L. Xiaohe, L. Yadong, *Mater. Chem. Phys.* **86**, 409 (2004)
9. P. Chen, S.J. Chua, Y.D. Wang, M.D. Sander, C.G. Fosta, *Appl. Phys. Lett.* **87**, 143111 (2005)
10. L. Jiang, Z. Cui, *Polym. Bull.* **56**, 529 (2006)
11. H. Yan, L. Zhang, J. Shen, Z. Chen, G. Shi, B. Zhang, *Nanotechnology* **17**, 3446 (2006)
12. W. Lee, R. Scholz, K. Nielsch, U. Gösele, *Angew. Chem., Int. Ed. Engl.* **44**, 6050 (2005)
13. M. Steinhart, J.H. Wendorff, A. Greiner, R.B. Wehrspohn, K. Nielsch, J. Schilling, J. Choi, U. Gösele, *Science* **296**, 1997 (2002)
14. A. Johansson, T. Törndahl, L.M. Ottosson, M. Boman, J.-O. Carlsson, *Mater. Sci. Eng., C, Biomim. Mater., Sens. Syst.* **23**, 823 (2003)
15. J.W. Elam, A. Zinovev, C.Y. Han, H.H. Wang, U. Welp, J.N. Hryn, M.J. Pellin, *Thin Solid Films* **515**, 1664 (2006)
16. G. Koh, S. Agarwa, P.S. Cheow, C.-S. Toh, *Electrochim. Acta* **53**, 803 (2007)
17. R. Singh, P.P. Sharma, R.E. Baltus, I.I. Suni, *Sens. Actuators B, Chem.* **145**, 98 (2010)
18. L. Liu, N. Jia, Q. Zhou, M. Yan, Z. Jiang, *Mater. Sci. Eng., C, Biomim. Mater., Sens. Syst.* **27**, 57 (2007)
19. G.D. Sulka, K. Hnida, *Nanotechnology* **23**, 075303 (2012)
20. G.D. Sulka, in *Nanostructured Materials in Electrochemistry*, ed. by A. Eftekhari (Wiley-VCH, Weinheim, 2008), pp. 1–116
21. M. Jaafar, D. Navas, M. Hernández-Vélez, J.L. Baldonado, M. Vázquez, A. Asenjo, *Surf. Sci.* **603**, 3155 (2009)
22. H. Masuda, K. Kanezawa, K. Nishio, *Chem. Lett.* **31**, 1218 (2002)
23. H. Asoh, K. Nishio, M. Nakao, T. Tamamura, H. Masuda, *J. Electrochem. Soc.* **148**, B152 (2001)
24. H. Masuda, K. Yasui, Y. Sakamoto, M. Nakao, T. Tamamura, K. Nishio, *Jpn. J. Appl. Phys.* **40**, L1267 (2001)
25. H. Asoh, S. Ono, T. Hirose, M. Nakao, H. Masuda, *Electrochim. Acta* **48**, 3171 (2003)
26. H. Masuda, H. Asoh, M. Watanabe, K. Nishio, M. Nakao, T. Tamamura, *Adv. Mater.* **13**, 189 (2001)
27. J. Choi, J. Schilling, K. Nielsch, R. Hillebrand, M. Reiche, R.B. Wehrspohn, U. Gösele, *Mater. Res. Soc. Symp. Proc.* **722**, L5.2.1 (2002)
28. W. Lee, R. Ji, C.A. Ross, U. Gösele, K. Nielsch, *Small* **2**, 978 (2006)
29. G.D. Sulka, K.G. Parkoła, *Thin Solid Films* **515**, 338 (2006)
30. K. Lee, Y. Tang, M. Ouyang, *Nano Lett.* **8**, 4624 (2008)
31. G.D. Sulka, S. Stroobants, V. Moshchalkov, G. Borghs, J.-P. Celis, *J. Electrochem. Soc.* **149**, D97 (2002)
32. G.D. Sulka, W.J. Stępniewski, *Electrochim. Acta* **54**, 3683 (2009)
33. M. Almasi Kashi, A. Ramazani, *J. Phys. D, Appl. Phys.* **38**, 2396 (2005)
34. P. Bocchetta, C. Synseri, A. Bottino, G. Capannelli, G. Chavarotti, S. Piazza, F. di Quarto, *J. Appl. Electrochem.* **32**, 977 (2002)
35. A.-P. Li, F. Müller, A. Birner, K. Nielsch, U. Gösele, *Adv. Mater.* **11**, 483 (1999)
36. R. Zhang, K. Jiang, G. Ding, *Thin Solid Films* **518**, 3797 (2010)
37. L. Zaraska, G.D. Sulka, M. Jaskuła, *Surf. Coat. Technol.* **204**, 1729 (2010)
38. L. Zaraska, G.D. Sulka, M. Jaskuła, *J. Phys. Conf. Ser.* **146**, 012020 (2009)
39. K. Schwirn, W. Lee, R. Hillebrand, M. Steinhart, K. Nielsch, U. Gösele, *ACS Nano* **2**, 302 (2008)
40. E. Ciepiela, L. Zaraska, G.D. Sulka, in *Building a National Distributed e-Infrastructure—PL-Grid—Scientific and Technical Achievements*, ed. by M. Bubak, T. Szepieniec, K. Wiatr (Springer, Berlin, 2012), pp. 240–251
41. E. Ciepiela, P. Nowakowski, J. Kocot, D. Hareźlak, T. Gubala, J. Meizner, M. Kasztelnik, T. Bartynski, M. Malawski, M. Bubak, in *Building a National Distributed e-Infrastructure—PL-Grid—Scientific and Technical Achievements*, ed. by M. Bubak, T. Szepieniec, K. Wiatr (Springer, Berlin, 2012), pp. 228–239
42. E. Ciepiela, L. Zaraska, G.D. Sulka, Implementation of algorithms of quantitative analysis of the grain morphology in self-assembled hexagonal lattices according to Hillebrand method. Executable publication powered by GridSpace2 platform, hosted in Academic Computer Centre CYFRONET AGH. <http://gs2.cyfronet.pl/epapers/hillebrand-grains/>
43. P. Nowakowski, E. Ciepiela, D. Hareźlak, J. Kocot, M. Kasztelnik, T. Bartyński, J. Meizner, G. Dyk, M. Malawski, *Proc. Comput. Sci.* **4**, 608 (2011)
44. ImageJ, National Institute of Mental Health, Bethesda, MD, USA. <http://rsb.info.nih.gov/ij>
45. J.P. O'Sullivan, G.C. Wood, *Proc. R. Soc. Lond. A* **317**, 511 (1970)
46. K. Ebihara, H. Takahashi, M. Nagayama, *J. Met. Finish. Soc. Jpn.* **34**, 548 (1983)
47. S.-K. Hwang, S.-H. Jeong, H.-Y. Hwang, O.-J. Lee, K.-H. Lee, *Korean J. Chem. Eng.* **19**, 467 (2002)
48. W.J. Stępniewski, Z. Bojar, *Surf. Coat. Technol.* **206**, 265 (2011)
49. R. Hillebrand, F. Muller, K. Schwirn, W. Lee, M. Steinhart, *ACS Nano* **2**, 913 (2008)